J. Fluid Mech. (1972), *vol.* 51, *part* 3, *pp.* 545–569
Printed in Great Britain

Turbulent boundary layer on a rotating helical blade

By B. LAKSHMINARAYANA, A. JABBARI AND H. YAMAOKA
Department of Aerospace Engineering, The Pennsylvania State University

(Received 12 July 1971 and in revised form 27 September 1971)

This paper investigates the boundary-layer characteristics on a helical blade of large chord length, enclosed in an annulus and rotating in a fluid otherwise at rest. The three-dimensional form of momentum integral equations is derived, and used to predict the boundary-layer growth and limiting streamline angles on the blade surface. The measurements are in general agreement with the predictions. The wall shear stress correlation, which includes both Reynolds number and rotation parameters, valid for a rotating blade operating at zero pressure gradient, is derived. Radial and tangential velocity profiles, the tangential component of turbulence intensity and blade static pressures are measured at several locations on the blade surface. The nature of flow near the blade tip is discussed. An expression for the radial velocity profile, valid in the outer region of the boundary layer, is derived theoretically.

1. Introduction

The boundary layer that develops on the blades of rotating fluid machinery (as e.g. with a compressor, turbine or helicopter blade) is not two-dimensional. There are centrifugal and Coriolis forces, which, in addition to pressure and viscous forces, make the direction of the flow inside the boundary layer different from the flow outside, thus forming a three-dimensional flow configuration. The following are the rotating boundary layers of this nature studied previously: (i) laminar boundary layers on a rotating blade of small chord length (Horlock & Wordsworth 1965; Fogerty 1951; Banks & Gadd 1962), (ii) turbulent boundary layers on axisymmetric bodies such as a disk or cylinder (von Kármán 1946; Cham & Head 1969; Banks & Gadd 1962), (iii) turbulent boundary layers in a centrifugal impeller, where the rotation is about an axis perpendicular to the flow (Johnston 1970; Moore 1969).

Lack of information about the boundary-layer characteristics of a rotating blade of large chord length (as used e.g. in rocket feed pumps: Lakshminarayana 1970) prompted this investigation. But, even though it is confined to such a configuration, the theoretical and experimental results on boundary-layer growth, velocity profiles, wall shear stress and turbulence intensities are widely applicable to other types of rotating boundary layers: that on turbomachinery blades has many three-dimensional features in common with, e.g., geophysical flows. A rocket pump inducer is usually an axial pump runner, having very high solidity (chord/

spacing), and very low aspect ratio (height/chord) blades, and operates at very low coefficient (ratio of inlet velocity to blade speed); the present study of the turbulent boundary layer on a single blade is the first step in a programme to find the information necessary to predict the flow in fluid machinery, such as a rocket pump inducer, that is dominated by viscous and turbulence effects.

The turbulent-boundary-layer characteristics of a rotating blade of large chord length, enclosed in an annulus as shown in figure 1, are investigated by both analysis and experiment. The blade rotates with an angular velocity Ω in a fluid otherwise at rest. The axial velocities are thus entirely due to frictional effects, and the pressure gradients are zero everywhere in the free stream. In §2 a flow model, governing equations and approximate methods of solutions are proposed; in §§3 and 4 there is a detailed presentation of the experimental programme and results, including velocity profiles, boundary-layer growth, and nature of the flow in the tip region; §§5 and 6 include general discussion and conclusions.

2. Theoretical considerations

2.1. *Flow model and governing equations*

For the purpose of flow analysis, the helical surface (figure 1), whose pitch is very small, is approximated by a flat circular plate with a leading and trailing edge. The calculation makes use of this, but the asymmetry of the flow that would prevail in the case of a helical blade is taken into account (i.e. it is assumed that

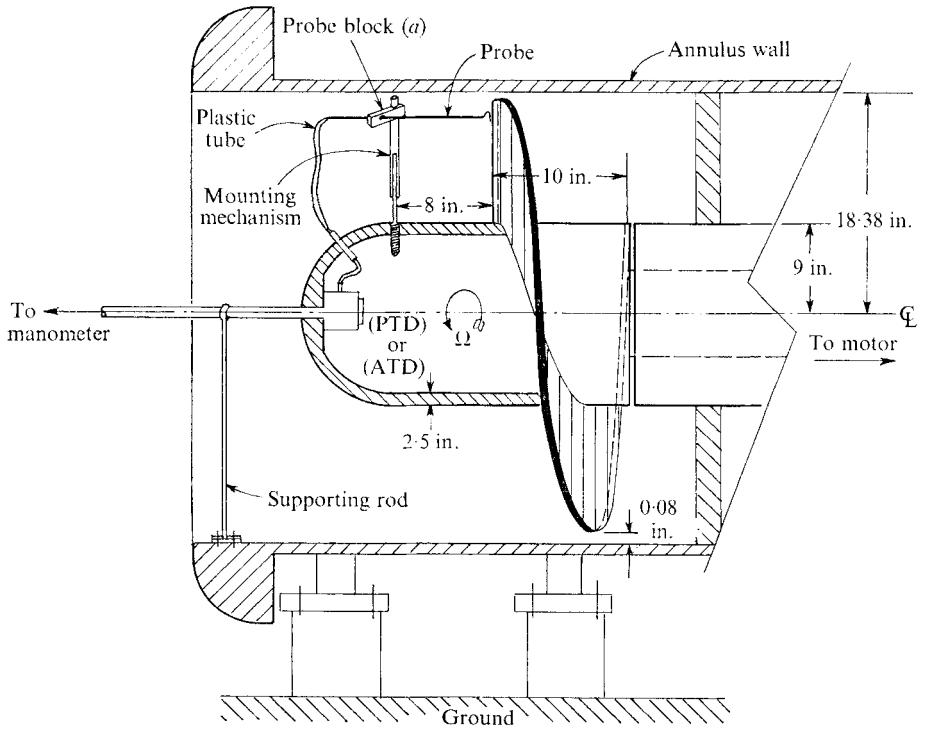

FIGURE 1. Schematic of the test assembly.

the trailing edge does not influence the leading edge). This model is similar to those of Banks & Gadd (1962).

A rotating cylindrical co-ordinate system (r, θ, z), as indicated in figure 2, is chosen. In the framework of boundary-layer theory, it is assumed that the pressure gradient of the main flow is imposed on the viscous layer near the wall.

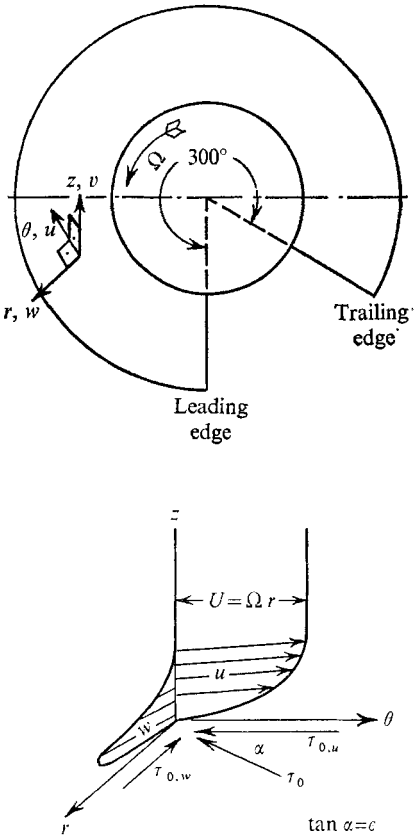

FIGURE 2. Co-ordinate system: nature of cross- and main-flow velocity profiles.

That assumption implies, in this case, that grad $P/\rho = 0$. Equations of mean motion for turbulent flow on a rotating helical blade can thus be written as

$$\frac{1}{r}\frac{\partial u}{\partial \theta} + \frac{\partial v}{\partial z} + \frac{\partial w}{\partial r} + \frac{w}{r} = 0, \tag{1}$$

$$\frac{u}{r}\frac{\partial u}{\partial \theta} + v\frac{\partial u}{\partial z} + w\frac{\partial u}{\partial r} - \frac{w}{r}(2\Omega r - u) = \frac{1}{\rho}\frac{\partial \tau_u}{\partial z}, \tag{2}$$

$$\frac{u}{r}\frac{\partial w}{\partial \theta} + v\frac{\partial w}{\partial z} + w\frac{\partial w}{\partial r} - \frac{(\Omega r - u)^2}{r} = \frac{1}{\rho}\frac{\partial \tau_w}{\partial z}, \tag{3}$$

where u, v, w are mean velocities in θ, z and r directions, Ω is the angular velocity of the blade, r is the local radius and τ_u and τ_w are shear stress in the direction of

u and w. The flow is assumed to be incompressible, and steady relative to the blade.

Momentum integral equations for the flow are

$$\frac{\partial \Theta_{11}}{\partial \theta} + 2\Theta_{12} + \frac{1}{r}\frac{\partial(\Theta_{12} r^2)}{\partial r} = \frac{\tau_{0,u}}{\rho \Omega^2 r}, \tag{4}$$

$$\frac{\partial \Theta_{21}}{\partial \theta} + \Theta_{22} - \delta_1^* + \Theta_{11} + \frac{1}{r}\frac{\partial(\Theta_{22} r^2)}{\partial r} = -\frac{\tau_{0,w}}{\rho \Omega^2 r}, \tag{5}$$

where the subscript 0 refers to values at the blade surface. The various boundary-layer thicknesses are defined by

$$\Theta_{11} = \frac{1}{(\Omega r)^2}\int_0^h u(\Omega r - u)\, dz, \tag{6}$$

$$\delta_1^* = \frac{1}{\Omega r}\int_0^h (\Omega r - u)\, dz, \tag{7}$$

$$\Theta_{22} = \frac{1}{(\Omega r)^2}\int_0^h w^2 dz, \tag{8}$$

$$\delta_2^* = \frac{1}{\Omega r}\int_0^h w\, dz, \tag{9}$$

$$\Theta_{12} = \frac{1}{(\Omega r)^2}\int_0^h (\Omega r - u)\, w\, dz, \tag{10}$$

$$\Theta_{21} = \frac{1}{(\Omega r)^2}\int_0^h wu\, dz. \tag{11}$$

The general velocity profiles on a rotating blade look like those of figure 2. The first general model, proposed by Prandtl, is

$$u/\Omega r = G(\eta), \quad w/\Omega r = \epsilon G(\eta)\, g(\eta), \tag{12), (13}$$

where $\eta = z/\delta$, $\epsilon = \tan\alpha$, and α is the limiting streamline angle (figure 2). ϵ is closely related to the frictional character of the flow. Given the available information on three-dimensional boundary layers, the following assumptions are made about the velocity profiles and shear stress (Mager 1951):

$$G = \eta^{\frac{1}{7}}, \quad g = (1-\eta)^2, \tag{14}$$

$$\tau_{0,u}/\rho(\Omega r)^2 = 0{\cdot}01255(R_{\Theta_{11}})^{-\frac{1}{4}}, \tag{15}$$

$$\tau_{0,w} = \epsilon \tau_{0,u}, \tag{16}$$

where $R_{\Theta_{11}} = \Omega r \Theta_{11}/\nu$ is the Reynolds number based on momentum thickness.

Since there are no pressure gradients in the flow, either Coles's profile or the $\frac{1}{7}$th profile can be used for the tangential velocity. Even though a theoretical expression for the radial velocity profile, valid in the outer layer, is derived in § 4.4 its incorporation in the momentum equations presents some difficulty, since the extent of the region in which this profile is applicable cannot be determined theoretically. The shear stress expression used is that for a stationary flat plate, and this does not take into account the rotational effects (see § 4.7).

Substituting (12)–(15) into (7)–(11), all the boundary-layer thicknesses can be expressed in terms of Θ_{11}. Substituting these, and the shear stress (16), into (4) and (5), one obtains

$$\frac{\partial\Theta_{11}}{\partial\theta}+2{\cdot}14\Theta_{11}\epsilon+0{\cdot}535r\epsilon\frac{\partial\Theta_{11}}{\partial r}+0{\cdot}535\Theta_{11}r\frac{\partial\epsilon}{\partial r}=0{\cdot}01255r\,(R_{\Theta_{11}})^{-\frac{1}{4}}, \tag{17}$$

$$2{\cdot}12\frac{\partial(\epsilon\Theta_{11})}{\partial\theta}-0{\cdot}2857\Theta_{11}+3{\cdot}3\Theta_{11}\epsilon^2+1{\cdot}11\epsilon^2 r\frac{\partial\Theta_{11}}{\partial r}$$
$$+2{\cdot}22\Theta_{11}\epsilon r\frac{\partial\epsilon}{\partial r}=-0{\cdot}01255\epsilon r\,(R_{\Theta_{11}})^{-\frac{1}{4}}. \tag{18}$$

Using the transformation $\Delta=\Theta_{11}(R_{\Theta_{11}})^{\frac{1}{4}}$, (17) and (18) can be simplified to give

$$\frac{\partial\Delta}{\partial\theta}+2{\cdot}526\Delta\epsilon+0{\cdot}535\epsilon r\frac{\partial\Delta}{\partial r}+0{\cdot}666\Delta r\frac{\partial\epsilon}{\partial r}=0{\cdot}0156r, \tag{19}$$

and

$$\Delta\frac{\partial\epsilon}{\partial\theta}+0{\cdot}8\,\epsilon\frac{\partial\Delta}{\partial\theta}-0{\cdot}1345\Delta+1{\cdot}47\Delta\epsilon^2+0{\cdot}415\epsilon^2 r\frac{\partial\Delta}{\partial r}+1{\cdot}06\,\Delta\epsilon r\frac{\partial\epsilon}{\partial r}+0{\cdot}0059\,\epsilon r=0. \tag{20}$$

Equations (19) and (20), with the boundary conditions $\Delta=\epsilon=0$ at $\theta=r=0$, provide the relationship for the limiting streamline angle α, and the momentum thickness Δ (or Θ_{11}), at various r and θ.

The analytical solution of (19) and (20) is extremely difficult. At any given radius, the momentum thickness should reach a constant value at a certain distance θ from the leading edge. Hence, an asymptotic solution valid for large θ is first derived in §2.2, assuming $\partial\Delta/\partial\theta=\partial\epsilon/\partial\theta=0$. Based on this analysis, a solution valid for the developing region is derived in §2.3. Then, in §2.4, an attempt is made to incorporate the effects of the laminar region near the leading edge of the blade .

The analysis of §§2.2–2.4 neglects the constraint of the annulus wall. On physical grounds, it can be argued that ϵ reaches zero, and that $\partial\Delta/\partial r$ is large near the blade tip (for the flow at the tip and a method of calculating Θ_{11} and ϵ there see §4.6).

2.2. *Asymptotic solution* $\partial/\partial\theta=0$

In §2.2 (19) and (20) are solved analytically under the condition $\partial/\partial\theta=0$. If $\partial/\partial\theta$ terms are dropped from (19) and (20), they should reduce to the equations of an axisymmetric disk; and Cham & Head (1969) concluded, from the numerical solution of these equations, that ϵ is nearly invariant with the radius, and that the assumption that $\partial\epsilon/\partial r=0$ results in only a 5% error in the prediction of Θ_{11}. The asymptotic solution of (19) and (20), based on this assumption, leads to

$$\Delta=5{\cdot}05\times10^{-3}r/\epsilon \quad\text{and}\quad \epsilon=0{\cdot}21. \tag{21}$$

2.3. *Solution for the developing region*

The solution of (19) and (20) in the developing region ($\partial/\partial\theta\neq0$) is based on the asymptotic solution. It is assumed that it has the form

$$\Delta=rF(\theta) \quad\text{and}\quad \epsilon=\epsilon(\theta). \tag{22), (23}$$

Hence, (19) and (20) reduce to

$$dF/d\theta + 3{\cdot}061F\epsilon = 0{\cdot}0156, \tag{24}$$

$$d\epsilon/d\theta = -0{\cdot}0184\epsilon/F + 0{\cdot}135 + 0{\cdot}585\epsilon^2. \tag{25}$$

Equations (24) and (25) are solved numerically using the fourth-order Runge–Kutta method. The initial conditions are $F = \epsilon = 0$ at $\theta = 0$; the effect of constraint due to hub and annulus walls is neglected (see §4.6). The values of the

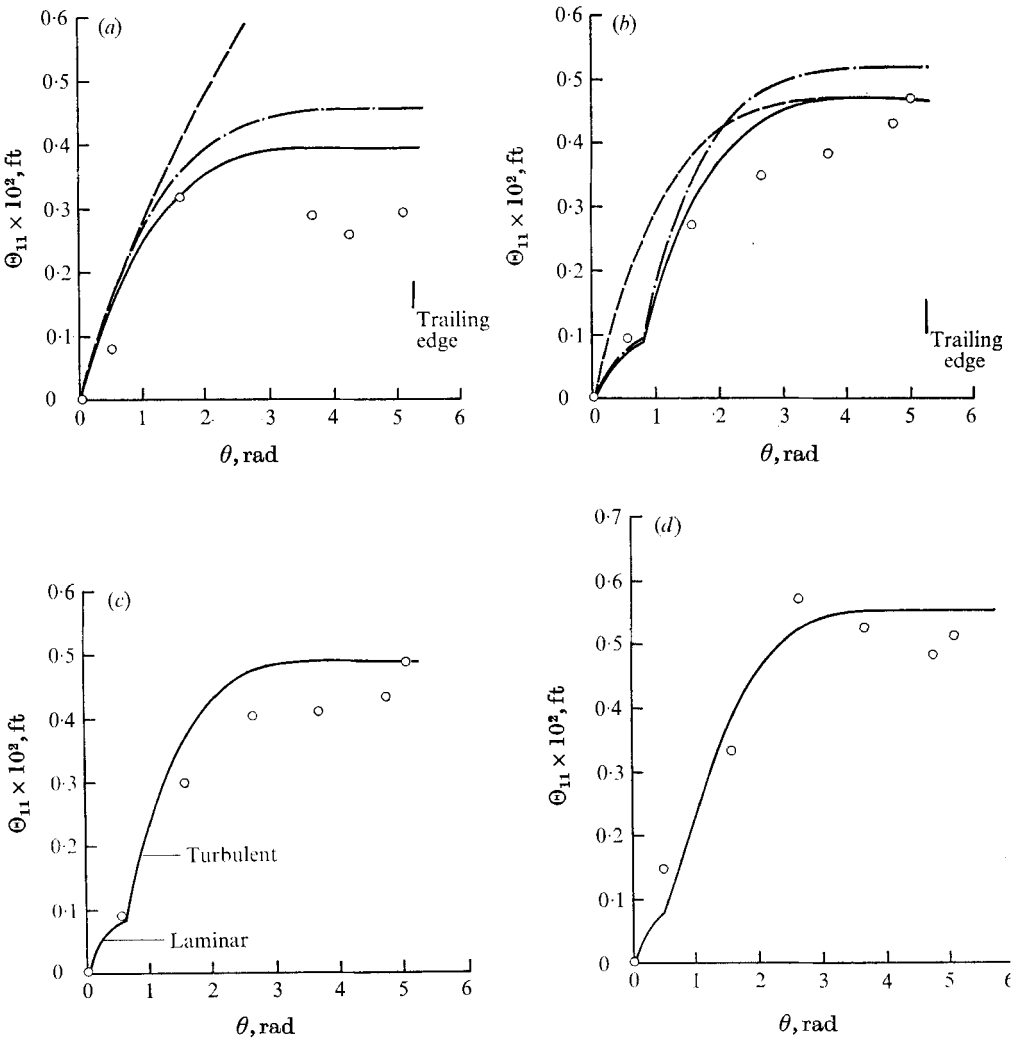

FIGURE 3. Tangential variation of momentum thickness Θ_{11}.

		(*a*)	(*b*)	(*c*)	(*d*)
Predicted	———	§2.3	§2.4	§2.4	§2,4
	—·—·—	§5	§5		
	- - - - - - -	Flat plate	§2.3 (fully turbulent)		
Measured		0	$R = 0{\cdot}55$	0·72	0·82	0·93

momentum thickness Θ_{11} at various distances from the leading edge, derived from

$$\Theta_{11} = rF(R_{\Theta_{11}})^{-\frac{1}{4}}, \tag{26}$$

are plotted in figure 3(*a*) for a rotating blade at $R = 0{\cdot}55$, $\Omega = 47\,\text{rad sec}^{-1}$ and $\nu = 160 \times 10^{-6}\,\text{ft}^2\,\text{sec}^{-1}$. The corresponding ϵ distribution is plotted in figure 4(*a*). Both the plots are for fully turbulent flow. The asymptotic values of Θ_{11} derived from this numerical solution are the same as those obtained from (21). The analytical solution of (24) and (25), neglecting second-order terms such as ϵ^2 and ϵF, gives $F = 0{\cdot}0156\theta$ and $\epsilon = 0{\cdot}0621\theta$ near the leading edge.

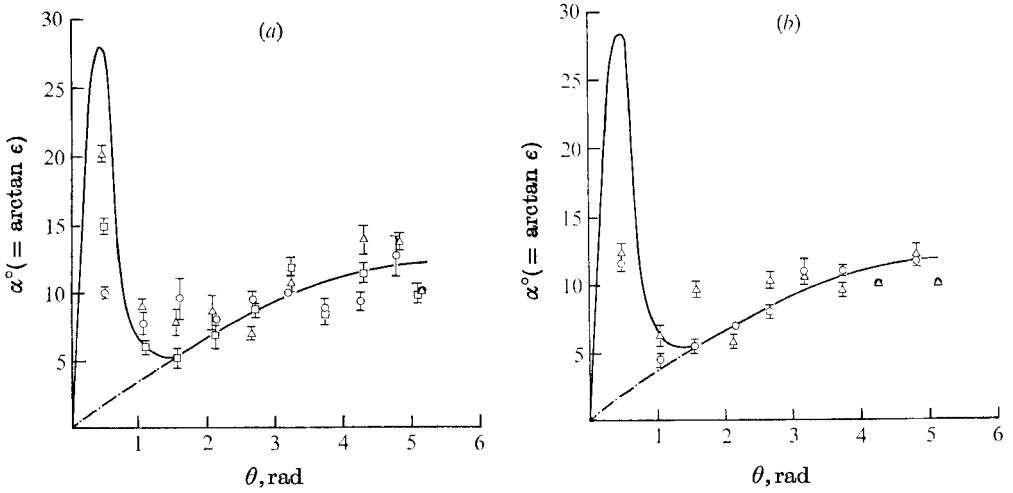

FIGURE 4. Variation of limiting streamline angle α (= arctan ϵ) with θ. Length of vertical line represents extent of scatter in data.

	Predicted		Measured		
	———	—·—·—	○	△	□
(*a*)	§2.4	§2.4 (fully turbulent)	$R = 0{\cdot}55$	0·74	0·84
(*b*)	§2.4	§2.4 (fully turbulent)	0·965	0·89	

The main conclusions of this analysis are (i) that ϵ and Δ vary linearly with θ near the leading edge, (ii) Θ_{11} reaches the asymptotic value at $\theta \simeq 3$rad, (iii) that the momentum thickness is much less than that of a corresponding (free-stream velocity Ωr) stationary flat plate (figure 3(*a*)), for $\theta > 0{\cdot}5$. The cross or radial flow, even though small in the case investigated here, has considerable effect in reducing the boundary-layer growth on a rotating blade.

2.4. *Effect of laminar region near the leading edge*

An exact analysis of the laminar boundary layer on a rotating propeller blade, by Banks & Gadd (1962), indicates that the limiting streamline parameter ϵ, near the leading edge is $1{\cdot}80\theta$, whereas the corresponding value derived for turbulent flow from (24) and (25) is $0{\cdot}0621\theta$. The fact that the radial flows are

likely to be much more severe in a laminar flow indicates that it is essential to incorporate these effects, if such there be, for accurate prediction of Θ_{11} and ϵ.

A slight modification is necessary to bring the prediction closer to reality. Using the critical Reynolds number criterion for a flat plate,

$$\Omega r^2 \theta_{\text{critical}}/\nu = 3 \times 10^5,$$

the extent of initial laminar region θ_{critical} is calculated. Banks & Gadd's analysis is then used to predict Θ_{11} and ϵ in the laminar region up to the point of transition. For $\theta > \theta_{\text{critical}}$, the turbulent flow equations (24), (25) are used to predict Θ_{11} and ϵ. The chord-wise (θ) variation of θ_{11} and ϵ so obtained are plotted in figures 3(*b*)–(*d*) and 4(*a*), (*b*) for various radii. The measured values of Θ_{11} and ϵ agree closely with the experiment (see §§4.1 and 4.5).

3. Experimental equipment and instrumentation

3.1. *Helical blade*

For the purpose of experiment, a helical blade of constant thickness, with an axial advance of 10 in., was built of fibreglass (see figure 1). The circumference of the blade was 300° from the leading edge. Metallic tubes of $\frac{1}{4}$ in. dia. were embedded in the blade at 30° intervals for a total of 10 stations. These tubes are used to determine the limiting streamline angle as well as blade static pressures. The measuring stations are designated in terms of θ and radial location (e.g. $\theta = 150°$ and $R = 0{\cdot}55$ refer to a tangential location 150° from the leading edge at a non-dimensional radius, with respect to tip radius, of 0·55). Unless otherwise stated, all measurements were carried out at the rotational speed of 450 rev/min corresponding to a Reynolds number of 7×10^5 based on the tip radius. Since all the measurements were taken relative to the rotating system, the devices of §§3.2–3.5 were used.

3.2. *Pressure transfer device*

This was a modified and improved version of the three channel PTD described by McCafferty (1967). The object was to transfer pressures from the rotating blade to a stationary precision manometer. The device was checked statically and dynamically, for any leak between the channels. The location of the PTD is shown in figure 1.

3.3. *Ammonia transfer device*

The ATD was similar to the PTD; it was used to transfer ammonia gas, from a stationary source of ammonia contained in a cylinder, to a desired location on the rotating blade surface. (For the method of measuring α, see §4.1.)

3.4. *Slip ring unit*

A rotating hot-wire probe was used for measuring the turbulence intensities in the tangential direction. The output was brought through a slip ring unit, whose inner ring was made out of silver, the noise-to-signal ratio of which was found to be extremely small. Effects of probe vibration were also found to be negligible.

3.5. *Probes*

Three different kinds of probe were used in measuring the stagnation pressure of the relative flow, flow angle within the boundary layer, and the wall shear stress. A two-hole yawmeter, made of 0·04 in. (outside) dia. tubes, was used for flow angle measurements. The pre-calibrated probe was aligned in the tangential direction, and the pressure differential recorded. The calibration curve ($2\Delta P/\rho V^2$ *vs.* α, where V is the resultant velocity $(u^2+w^2)^{\frac{1}{2}}$ at the measuring point) was then used to determine the flow angle (Jabbari 1969). The turbulence intensity in the tangential direction was measured by means of a hot-wire (tungsten) probe of 3μ dia. and a length-to-diameter ratio of 300. The constant-temperature hot-wire anemometer used was of Wyngaard–Lumley (1967) design. All three kinds of probe were installed on the same mounting mechanism for different measurements. Figure 1 shows a schematic diagram of the traversing device. The distance between the mounter, and the point at which the data were obtained was sufficient (8 in.) to ensure least interference with the flow in the boundary layer.

4. Experimental results and comparison with predictions

4.1. *Flow visualization and limiting streamline angles*

To determine the extent of the initial laminar region, a flow visualization method was adopted which used a sublimation technique. After several trials the technique of Richards & Burstall (1945) was found to be most suitable. The transition at mid radius ($R = 0{\cdot}75$) occurred at $\theta = 41°$, which corresponds to a Reynolds number of $2{\cdot}7 \times 10^5$. This is slightly lower than critical Reynolds number used for Θ_{11} and ϵ prediction in §2.4. The transition at all other radii occurred earlier than in the case of a flat plate, indicating that rotation effects an early transition. No laminar region exists near the hub tip locations of the blades. The sharp leading edge of the blade caused early transition to turbulent flow, but relaminarization occurred immediately at all radial positions, except near the hub and tip.

The limiting streamline angle α was determined using the ATD of §3.3. First, a number of small-diameter holes were drilled on the blade surface through the metallic tubes. Using the ATD, a small amount of ammonia gas at very low velocities was fed into the tubes at various tangential locations. A sheet of ozalid paper, sensitive to ammonia, was pasted along the edges of the static holes, so that traces of ammonia were recorded on it while the blade was in rotation. The amount of deflexion from the tangential direction gave the value of α at that location. This procedure was repeated several times at each point to make certain the angles obtained were accurate. The variation of α with θ is given in figure 4. The vertical lines indicate the amount of experimental scatter. This experimental scatter, however, is only a few degrees at the most.

Now compare the experimental and theoretical values of α plotted in figure 4. (i) It is seen that much larger values of α are obtained in the laminar region than in the turbulent region. This is in conformity with the analysis of Banks & Gadd (1962) for a screw propeller. (ii) At the trailing edge ($\theta > 5$ rad), a consistent

decrease in values of α is observed at all radii, accounting for the decay of the radial velocity as the flow leaves the trailing edge.

The analysis of §2 does not take into account the constraint of the annulus wall, so that it predicts $d\epsilon/dr = 0$. Experimental results seem to indicate that this is true at most of the radial locations except near the tip, where a decrease in α is observed (§4.6). Thus, it may be said that the theoretical prediction of ϵ is reasonably good everywhere, except near the hub and tip locations (figure 4).

4.2. *Blade static pressure*

The analysis of §2 is based on the assumption that the pressure gradient of the flow is zero everywhere in the field. To check this assumption, the static pressures were measured on the surface, using the PTD and the static holes drilled on the

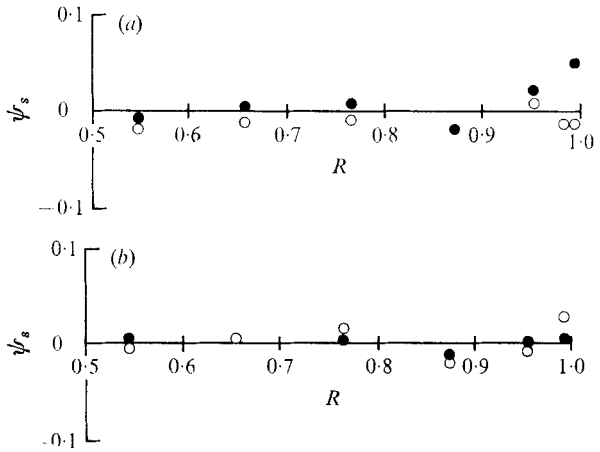

FIGURE 5. Blade static pressure (○, front; ●, back). (*a*) $\theta = 30°$, (*b*) $\theta = 210°$.

surface. The radial variations of the non-dimensionalized static pressure coefficient ψ_s at two typical locations are plotted in figure 5. ψ_s is defined as

$$\psi_s = 2gh/U_t^2, \tag{27}$$

where U_t is the tip velocity, and h is the static head. As figure 5 shows, the radial pressure gradient is negligibly small throughout the flow field, except, perhaps, near the tip (§4.6 gives the reasons for the appreciable radial pressure gradient near the tip).

4.3. *Tangential velocity profiles*†

The measured tangential velocity profiles at various tangential and radial locations of the blade are plotted in figures 6(*a*), (*b*). Near the leading edge of the blade at $\theta = 30°$ (figure 6(*a*)), the laminar type of profile exists at $R = 0{\cdot}72$ and 0·82. The measured values at these radial locations are compared with the theoretical profile of Banks & Gadd (1962). The agreement is good in the outer

† The boundary-layer data of §§4.3–4.7 supersede those of Jabbari (1969). Some of the measurements were repeated, few corrected for probe errors. Those wishing to obtain the new data should contact B.L.

region of the boundary layer, the departure being greatest near the blade surface. Since the boundary layer is very thin in this region, the experimental accuracy is poor near the blade surface. The turbulent velocity profiles measured at various radial and tangential locations (figures 6 (*a*), (*b*)) agree closely with the

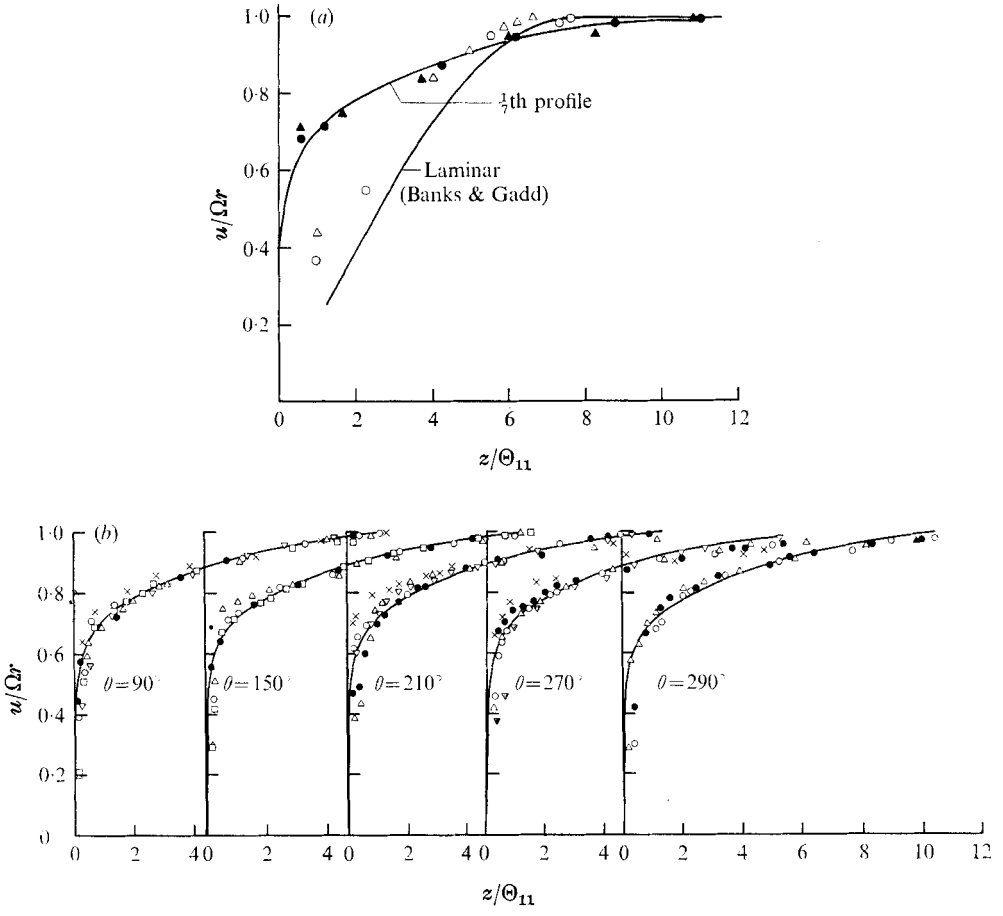

FIGURE 6. Tangential velocity profiles.

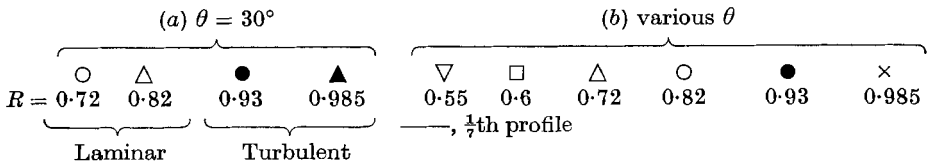

$\frac{1}{7}$th profile (or the Coles profile at zero pressure gradient). Appreciable departure from the assumed profile was observed only near the blade tip, and close to the wall. The free-stream velocity is $U = \Omega r$ everywhere, except at the tip, where a core region, rotating with a velocity $U_c < \Omega r$, is observed. This core velocity is used for non-dimensionalizing the local velocity for (flow measurement near the tip, see §4.6). The scatter in the gathered data are larger than those normally

observed in profile measurements on a stationary body. Considering the difficulties involved in taking the measurements from a rotating probe, they show remarkable agreement with the power law profile.

The mean velocity data u are shown in the conventional 'law of the wall' form in figure 7. The experimental data seem to fit the logarithmic velocity distribution of the form

$$u/u^* = A \log_{10} z^+ + B \tag{28}$$

where $$\frac{u}{u^*} = \frac{1{\cdot}412}{\sqrt{C_f}} \frac{u}{U}, \quad U = \Omega r \text{ except at } R = 0{\cdot}985, \quad z^+ = \frac{zu^*}{\nu}. \tag{29}$$

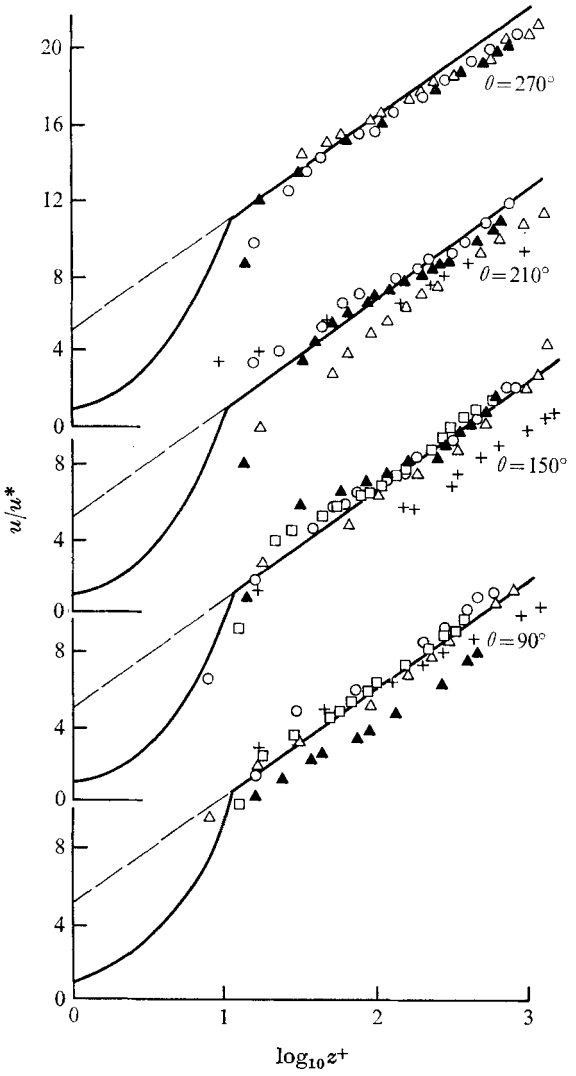

FIGURE 7. Test of the law of the wall for the tangential velocity profile. $\theta = 90°$, 150°, 210°, 270°. ———, $u/u^* = 5{\cdot}8 \log_{10} z^+ + 5{\cdot}0$.

□	▲	○	△	+
$R = 0{\cdot}6$	0·72	0·83	0·93	0·985

The skin friction coefficients C_f used in these plots are the experimental values derived from Preston's (1954) method, and described in §4.7. The data seem to fit (28) with $A = 5{\cdot}8$ and $B = 5{\cdot}0$. The departure of the data from this relationship occurs mostly at the hub and tip of the blade. The experimental accuracy of these measurements is poor in the hub region where the boundary layer is very thin, whereas the free-stream velocity at the tip does not reach the value Ωr (§4.6). The difficulty in establishing the exact value of the free-stream velocity

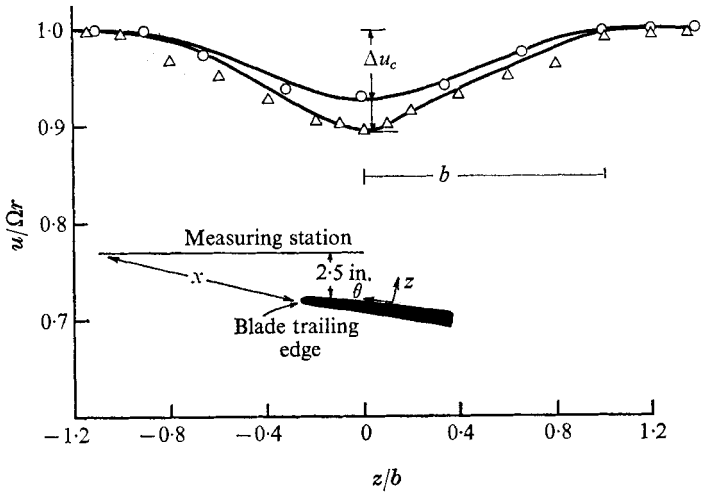

FIGURE 8. Wake profile (tangential component) downstream of the blade trailing edge. ———, $1-\Delta u_c[1-(z/b)^{\frac{3}{2}}]^2$. △, $x/l = 0{\cdot}25$, $R = 0{\cdot}975$, $b = 1{\cdot}63$ in; ○, $x/l = 0{\cdot}26$, $R = 0{\cdot}775$, $b = 1$ in.

might have resulted in the departure of the data at $R = 0{\cdot}985$ from (28). Nevertheless, it is clear that the tangential component follows the law of the wall at most of the blade locations. The two-dimensional logarithmic velocity profile does indeed give good results in this particular three-dimensional configuration (consistent with Prahlad's (1968) conclusion that the law of the wall is valid in three-dimensional boundary layers).

The stagnation pressures of the relative flow downstream of the trailing edge were obtained with the aid of a rotating probe and probe holder developed by McCafferty (1967). The wake velocity profiles derived from these measurements at two radii are plotted in figure 8, where l refers to local chord length, which corresponds to the length of the flat plate. The measured wake profile (tangential component) shows good agreement with the theoretical profile for two-dimensional wakes proposed by Schlichting (1960, p. 601); but the decay of the wake seems to be faster than that observed in the case of a flat plate (Fage 1933). The radial velocities present in the wake are largely responsible for its faster diffusion.

4.4. *Radial velocity profiles*

The measured radial and tangential velocity components are shown in a polar plot in figure 9. The measured radial velocities are generally lower than those derived from Mager's profile ((12)–(14)). Furthermore, it is found that the radial velocities in this case are generally higher than those of the axisymmetric disk (Cham & Head 1969), and that they do not follow the triangular representation of Johnston (1960). Clearly, the maximum radial velocity (about 14–18 % of

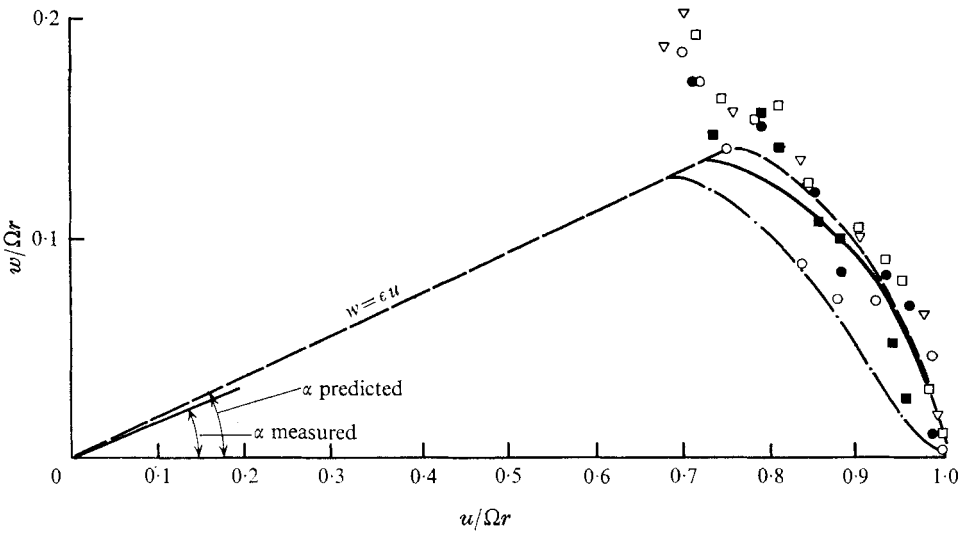

FIGURE 9. Plot of polar velocities.

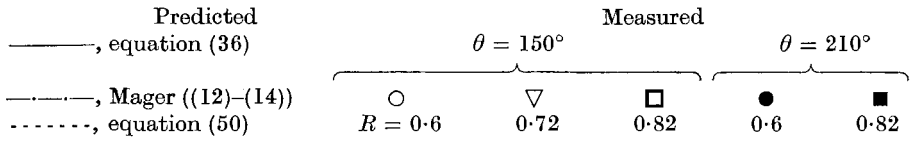

the free-stream velocity) occurs very near the blade surface. The location of the maximum velocity (i.e. $u/\Omega r = 0{\cdot}7$, in this case) seems to agree with Cham & Head's (1969) measurement on a disk. It is very unlikely that either Johnston's (1960) or Mager's model is valid in a rotation-induced three-dimensional boundary layer, even though Cham & Head (1969) report close agreement with Mager's profile for an axisymmetric disk flow. With this in mind a derivation of the nature of the cross or radial flow profile, valid for the boundary layer on a rotating blade, is now attempted.

The analysis is based on the developed flow (i.e. $\partial/\partial\theta = 0$), and is valid for the outer layer, where shear stresses can be neglected. By neglecting $\partial/\partial\theta$ terms in (2) and (3), and eliminating v from them one can obtain

$$w\left(\frac{\partial w}{\partial r}\frac{\partial u}{\partial z}-\frac{\partial u}{\partial r}\frac{\partial w}{\partial z}\right)+2\Omega\left(u\frac{\partial u}{\partial z}+w\frac{\partial w}{\partial z}\right)-\frac{u}{r}\left(u\frac{\partial u}{\partial z}+w\frac{\partial w}{\partial z}\right)=\Omega^2 r\frac{\partial u}{\partial z}. \qquad (30)$$

It is supposed that the radial velocity component is related to the tangential velocity component by

$$w/\Omega r = Bf(u/\Omega r), \tag{31}$$

where B is a constant. Hence,

$$\frac{\partial w}{\partial r} = B\Omega f + B\frac{\partial u}{\partial r}f' - B\frac{u}{r}f' \quad \text{and} \quad \frac{\partial w}{\partial z} = Bf'\frac{\partial u}{\partial z}. \tag{32), (33}$$

Substituting (31)–(33) into (30), after some simplification one obtains

$$B^2\left\{f^2 + 2\left(1-\frac{u}{\Omega r}\right)ff'\right\} = \left(1-\frac{u}{\Omega r}\right)^2, \tag{34}$$

where f' is the derivative of f with respect to $u/\Omega r$. Since $f = 0$ when $u = \Omega r$, the solution of (34) is

$$f = \left[\frac{u}{\Omega r}\left(1-\frac{u}{\Omega r}\right)\right]^{\frac{1}{2}}. \tag{35}$$

The measured data in the outer layer, shown in figure 9, seem to fit

$$\frac{w}{\Omega r} = 0{\cdot}3\left[\frac{u}{\Omega r}\left(1-\frac{u}{\Omega r}\right)\right]^{\frac{1}{2}}. \tag{36}$$

It is evident that the behaviour of the rotation-induced radial or cross-flow profile is different from that of cross-flow induced in a stationary system owing e.g. to free-stream turning. Additional data are needed before any further analysis can be made. The agreement of the measured data (figure 9) with the various models described is poor at the buffer layer, which overlaps between the collateral region and the outer layer. The reason for this is experimental inaccuracy close to the wall, and the inadequacy of the inviscid model in this region. It seems that the equations of motion can be solved, for the buffer layer, only numerically, and given some physically realistic model of the turbulence: Nash (1969) and Bradshaw (1971) have made some progress in this direction. One can conclude that, apparently, the outer-layer profile in a rotating boundary layer (without pressure gradients) can be adequately represented by

$$w/\Omega r = C_1[(1-u/\Omega r)(u/\Omega r)]^{\frac{1}{2}}, \tag{37}$$

and the collateral region by $w = \epsilon u$. (38)

4.5. *Momentum thickness* Θ_{11}

The experimental values of momentum thickness Θ_{11} are derived by numerical integration of (6), using the measured velocity profile. These are compared with the predicted values in figures 3(*a*)–(*d*). The predictions are good at all radial locations, except near the hub ($R = 0{\cdot}55$, $\theta > 3$), where the profile measurements are not very accurate for reasons mentioned above, and owing to complex interaction of the hub boundary layer and the blade boundary layer at this location. It is observed, furthermore, that there is a sudden increase in Θ_{11} near the trailing edge. This is caused by a decrease in ϵ at these locations (see figures 4(*a*), (*b*)),

and this effect can be attributed to wake effect, where the radial velocities decay very fast. The agreement between the theory and experiment at the tip ($R = 0{\cdot}985$) is poor (see §4.6).

4.6. *Flow in the tip region*

In a region close to the annulus wall, tangential velocity component distribution is found to be very different from other radial locations. As an example, consider the measured distribution of the tangential velocity component at $\theta = 180°$

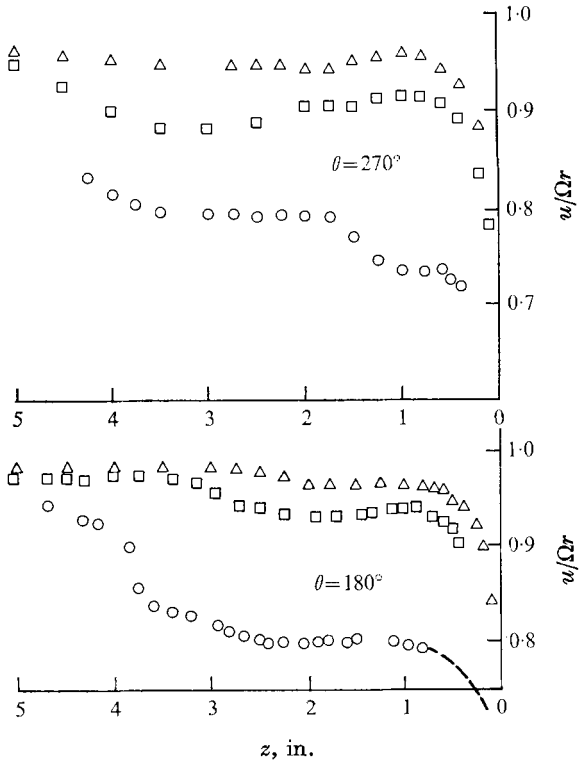

FIGURE 10. Tangential profiles in the tip region.

△	□	○
$R = 0{\cdot}93$	0·955	0·985

and $R = 0{\cdot}985$ shown in figure 10. It is seen that, as the distance from the blade surface increases, the tangential velocity component increases, and reaches a value different from the free-stream velocity Ωr. This region is followed by one where the tangential velocity component changes very little, and may be considered constant. Then the tangential velocity component increases, approaching the free-stream value asymptotically, this behaviour is also observed at $R = 0{\cdot}955$ and 0·93 (figure 10), and at other θ locations.

Bearing these points in mind, the tip region can be divided in three. (i) Near the blade surface, effects of the viscosity of the fluid cannot be neglected: this

is the blade boundary layer. The boundary-layer thickness is determined by the location at which the tangential velocity component reaches a constant value. (ii) The region adjoining the blade boundary layer, in which the tangential velocity component is constant, is the 'core region'. (iii) The region outside the core region, where the tangential velocity component increases to the free-stream value Ωr, is the 'interference region'.

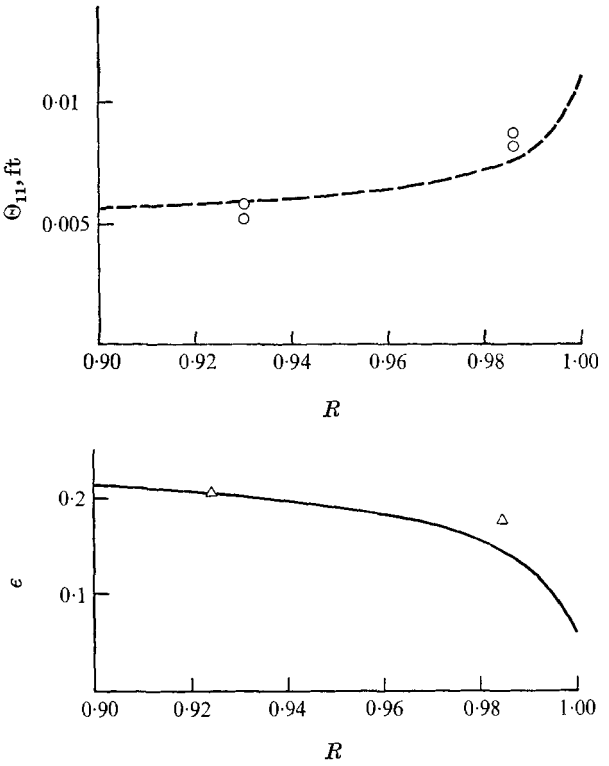

FIGURE 11. Θ_{11} and ϵ variation near the tip.

Predicted: ——— ϵ, – – – – – –, Θ_{11}
Measured: △, ϵ ($\theta = 270°$) ○, Θ_{11} ($\theta = 150°, 270°$)

(i) *Flow in the blade boundary layer.* The boundary-layer thickness at the tip is determined by a location where the tangential velocity component approaches to a constant value U_c, which is smaller than the free-stream value Ωr. It is supposed that the pressure does not vary across the boundary layer. Since the radial velocity component is zero at the edge of the boundary layer, the radial pressure gradient is given by

$$\frac{1}{\rho}\frac{\partial p}{\partial r} = \frac{1}{r}(\Omega r - U_c)^2 \quad \text{or} \quad \frac{\partial \psi_s}{\partial R} = \frac{2}{R}\left(R - \frac{U_c}{\Omega r_t}\right)^2. \qquad (39), (40)$$

The tangential velocity measurements (figure 10) indicate that the radial pressure gradient increases as the annulus wall is approached. Figure 8 clearly shows the increase in blade static pressure as the radial distance increases. This agrees

with the result obtained from (39), based on measurement of U_c. An attempt has been made to calculate ϵ and Θ_{11} near the tip region, by allowing for a radial pressure gradient neglected in the analysis of §2. If the radial pressure gradient term $(1/\rho)(\partial p/\partial r)$ is introduced in (3), and if this term is carried through in (5) and (18), the additional term $-2{\cdot}43(\Delta/R)(\partial\psi_s/\partial R)$ appears on the right-hand side of (20). No prediction of the core velocity U_c, or $\partial\psi_s/\partial R$, was forthcoming

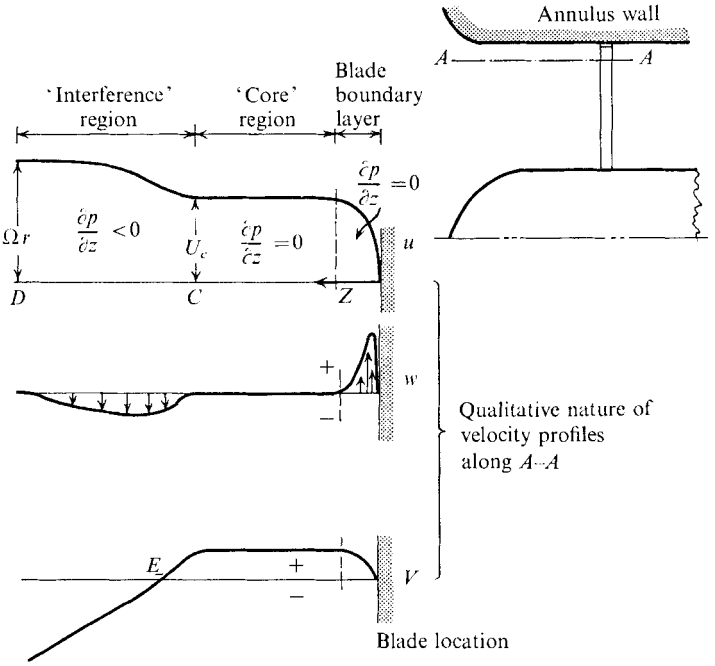

FIGURE 12. Qualitative nature of velocity profiles in the tip region.

so that an attempt was made to explain the large increase in Θ_{11}, and decrease in ϵ, measured near the tip, by using the measured U_c in (40). Equation (19), and the modified (20), were solved numerically to derive Θ_{11} and ϵ near the tip for asymptotic conditions $(\partial/\partial\theta = 0)$. The boundary conditions used for the solution of (19) and (20) are those given by (21) at $R = 0{\cdot}9$. The calculated and measured Θ_{11} and ϵ, plotted in figure 11, show good agreement. It is evident that, for accurate prediction of the boundary-layer characteristics near the tip, it is essential to include the pressure gradient term and the consequent decreases in ϵ towards the tip.

(ii) *Flow in the core region* $(\partial u/\partial z = 0)$. It is clear, from (2), that $w = 0$ for the developed case. Thus $\partial p/\partial z = \partial v/\partial z = 0$.

(iii) *Flow in the interference region.* In the blade boundary layer, the effect of rotation is to induce a positive or outward radial velocity. Because of the annulus wall, the radial flow at the tip is directed axially outward. This results in opposing flows, i.e. the axial flow at the outer edge of the interference region (point D in figure 12) is inward; whereas, at its inner edge (point C in figure 12), the same flow is outward. So the axial velocity component changes its sign in the

interference region. The interaction of the two opposing flows produces a radially inward flow. Figure 12 is a qualitative picture of velocity profiles in the tip region, based on the above heuristic argument.

4.7. *Wall shear stress measurements*

There has been discussion about how to measure the wall shear stress in three-dimensional boundary-layer flows: Pierce & Krommenhoek (1968) showed, by comparing it with the direct method that the preston tube technique is adequate; and one group used this technique for rotating boundary layers (Halleen & Johnston 1967). Here, too, the Preston tube technique was used: a pitot tube was

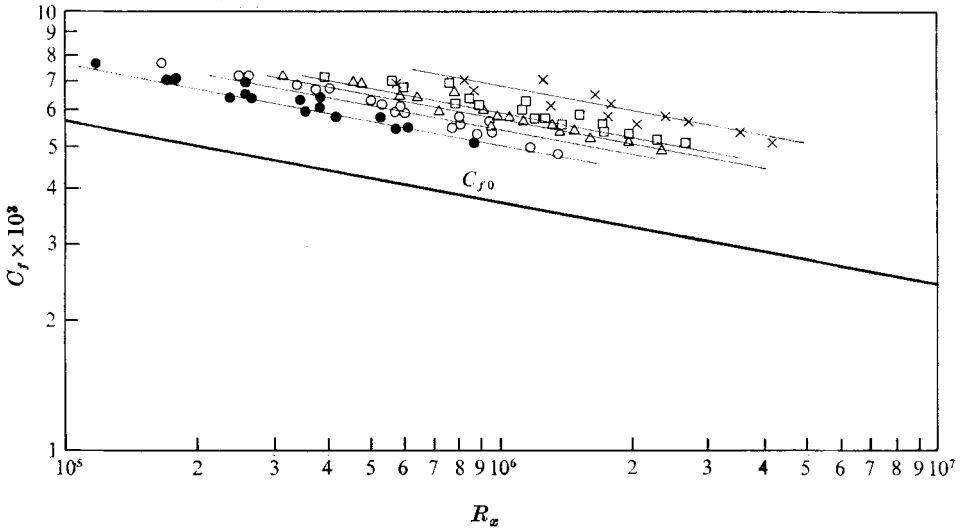

FIGURE 13. Coefficient of skin friction for a rotating blade. $R_x = \Omega r^2\Theta/\nu$.

———, Schlichting (equation (41))

Measured	●	○	△	□	×
	$\theta = 1{\cdot}04$	1·56	2·64	3·18	4·76 rad

mounted flush to the surface of the rotating helical blade, and, at each position, the Preston tube was aligned in the resultant flow direction, to measure the total pressure at that position. From the known static pressure distribution, a dynamic pressure was determined. The dynamic pressure was then related to the wall shear stress by the calibration scheme of Patel (1965).

Wall shear stress measurements were made at different rotational speeds of 200, 300, 400, 450, 600 and 700 rev/min by a Preston tube of $\frac{1}{16}$ in. (outside) dia. In figure 13, the skin friction coefficients (based on the resultant shear stress τ_0) are plotted against the Reynolds number based on the distance measured from the leading edge of the blade. The measured skin friction coefficient is much larger than the skin friction coefficient for a two-dimensional flat plate given by Schlichting,

$$C_{f_0} = 0{\cdot}0582 R_x^{-\frac{1}{5}}, \tag{41}$$

where R_x is the Reynolds number based on the distance from the leading edge $x = r\theta$, and the local velocity Ωr. Also, the measured values of C_f for the rotating blade show a consistent variation with θ, in that all the measured values, at any given θ, can be represented by parallel straight lines on the logarithmic plot (figure 13). So in addition to Reynolds number, the expression for the skin friction coefficient must include a parameter representative of rotation effects.

Even though the Coriolis force in the tangential direction is zero in the free stream, its value is non-zero inside the boundary layer; this tends to change the turbulence characteristics, and hence the shear stress. The most appropriate parameter for this case seems to be the ratio of the Coriolis to the inertial force.

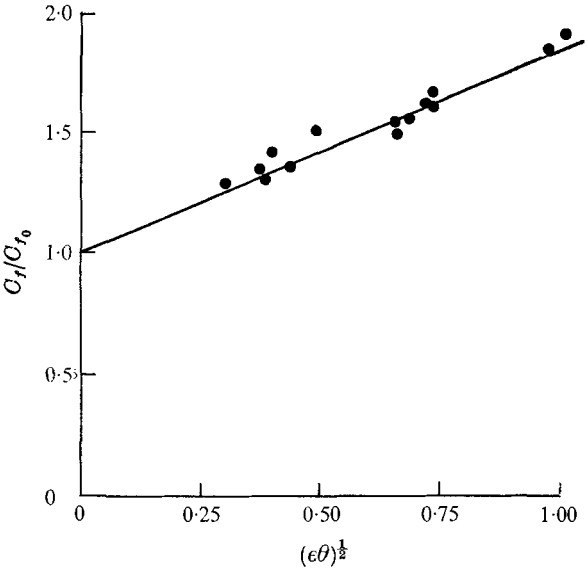

FIGURE 14. Ratio of skin friction coefficients C_f/C_{f_0} plotted against the rotation parameter $\epsilon\theta$ (θ rad). ———, equation (43); ●, measured (450 rev/min).

The Coriolis force inside the boundary layer in the tangential direction is $2\Omega w$, whereas the dominant inertial term in the *developing* region is $u(\partial u/\partial\theta)/r$. Furthermore,

$$\frac{1}{u}\frac{\partial u}{\partial\theta} \sim \frac{1}{\delta}\frac{\partial\delta}{\partial\theta},$$

as can be seen from (12)–(14). Furthermore, $\partial\delta/\partial\theta \sim \delta/\theta$ in the developing region. Hence, the ratio of Coriolis force to inertial force, which is a measure of the rotation effects, is

$$R_0 = \frac{2\Omega w}{u(\partial u/\partial\theta)/r} \sim \frac{2\Omega w}{u^2(\partial\delta/\partial\theta)/r\delta} \sim \epsilon\theta. \tag{42}$$

The skin friction data at 450 rev/min seem to fit (figure 14)

$$C_f/C_{f_0} = 1 + 0{\cdot}85\,(\epsilon\theta)^{\frac{1}{2}}, \tag{43}$$

which involves the required rotation parameter.

Equation (43), and the data plotted in figures 13 and 14, show considerable increase in skin friction coefficient for a rotating blade, as compared with a stationary flat plate with equivalent length $r\theta$, and free-stream velocity Ωr. McCroskey, Nash & Hicks (1971) reported increased skin friction stress on a rotating flat plate blade, using a numerical solution of Nash (1969), who integrated the equations of motion by a finite-difference method. The shear stress is

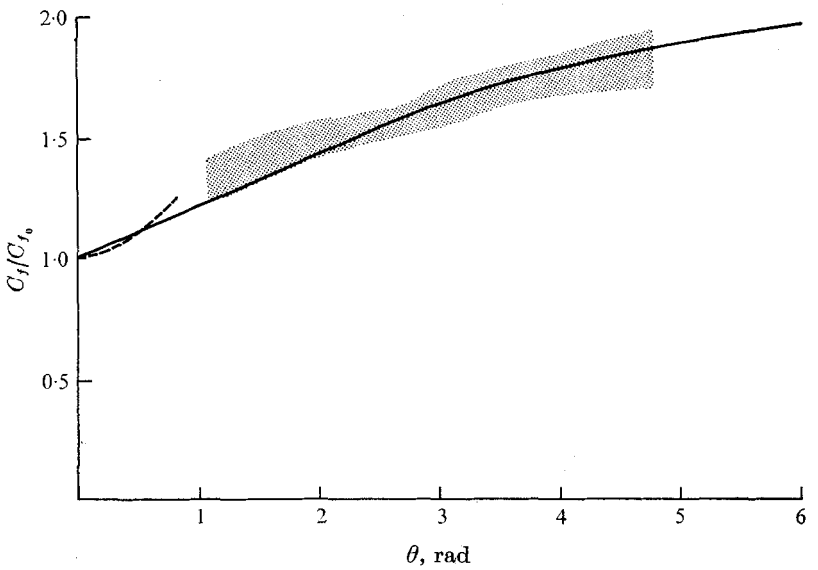

FIGURE 15. Ratio of skin friction coefficient C_f/C_{f_0} plotted against θ. ———, equation (43); – – – –, McCroskey *et al.* (1971); ▦, present measurements.

determined by the integration of the modified turbulent energy equation modified by the inclusion of empirical functions of a form which has proved successful in two dimensions, and somewhat successful with the stationary type of three-dimensional boundary layers; but its validity to rotating case has yet to be established. The predictions of McCroskey *et al.* (1971) are plotted against θ, the chord-wise angular location, in figure 15. Also plotted in this figure are the values obtained from (43), using predicted ϵ, and the authors' measurements. The agreement seems to be reasonably good.

For the developed flow ($\partial/\partial\theta = 0$), the skin friction coefficient must be represented by a quantity which does not include the distance from the leading edge. Plotted against Reynolds number based on local radius and local free-stream velocity in figure 16, it is well represented by

$$C_f = 0{\cdot}079(R_r)^{-\frac{1}{6}}, \tag{44}$$

where R_r is the Reynolds number (i.e. $\Omega r^2/\nu$).

Hence, the rotation effects on skin friction stress are large, and their inclusion is essential for accurate prediction of the boundary-layer characteristics. The correlations proposed are, in the developing region,

$$C_f = 0{\cdot}0582(\Omega r r\theta/\nu)^{-\frac{1}{6}}[1 + 0{\cdot}85(\epsilon\theta)^{\frac{1}{2}}], \tag{45}$$

and, in the developed region,

$$C_f = 0{\cdot}079(\Omega r^2/\nu)^{-\frac{1}{5}}. \tag{46}$$

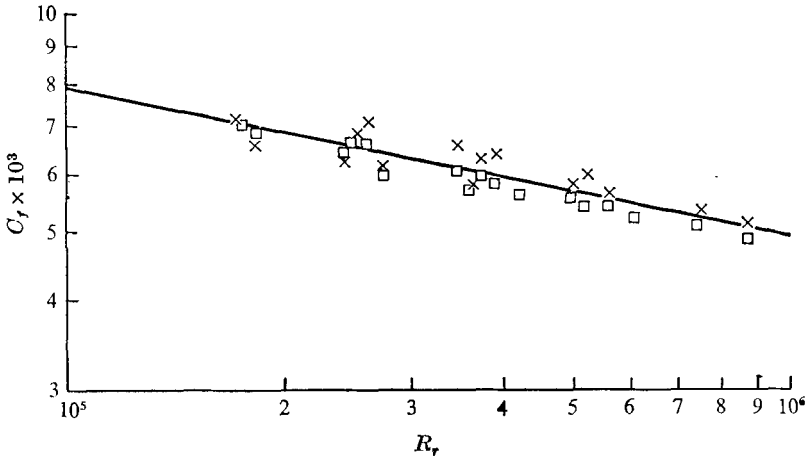

FIGURE 16. Plot of skin friction coefficient against Reynolds number based on local radius $R_r = \Omega r^2/\nu$. ——, equation (44). Measured: □, $\theta = 3{\cdot}18$ rad; ×, $\theta = 4{\cdot}76$ rad.

4.8. *Turbulence intensity*

To determine the nature and magnitude of turbulence intensity inside the boundary layer, an attempt is made to measure its tangential component $((\overline{u'^2})^{\frac{1}{2}}/\Omega r)$. Measurement of the other two components requires extremely sophisticated instrumentation and signal transmission.

The voltage sensed by a wire aligned in the radial direction is given by King's Law,

$$E^2 = E_0^2 + B[(u+u')^2 + (v+v')^2]^{\frac{1}{4}}, \tag{47}$$

where u', v' are fluctuations in the u and v velocity components, respectively. The angularity error is small, since the resultant flow deviation from the tangential direction is of the order of 10° in the turbulent regions of the blade (figures 4(*a*), (*b*)). Since axial velocity is small, and intensities are assumed to be low, (47) can be simplified to

$$E^2 = E_0^2 + B\sqrt{u}\left[1 + \frac{u'}{2u} + \frac{1}{4}\left(\frac{v}{u}\right)^2\right]. \tag{48}$$

The turbulence intensity in the tangential direction can then be expressed as

$$T = \frac{4\bar{E}e_{\text{rms}}}{\bar{E}^2 - E_0^2}\left[1 + \frac{1}{4}\left(\frac{v}{u}\right)^2\right], \tag{49}$$

where $\bar{E}, E_0$ are mean voltage and voltage at zero velocity respectively e_{rms} = r.m.s. value of the fluctuating voltage. Since $v/u \ll 1$, the turbulence intensities are derived by measuring e_{rms}, then using (49) and neglecting the term involving v/u.

The turbulence intensities measured at three locations are plotted in figure 17 and compared with the flat plate data of Klebanoff (1955). Their tangential

component is generally higher than that in the case of a flat plate, and is consistent with the shear stress measurements reported in §4.7, if it is assumed that the turbulence intensity is directly proportional to the local shear stress (Bradshaw, Ferris & Atwell 1967).

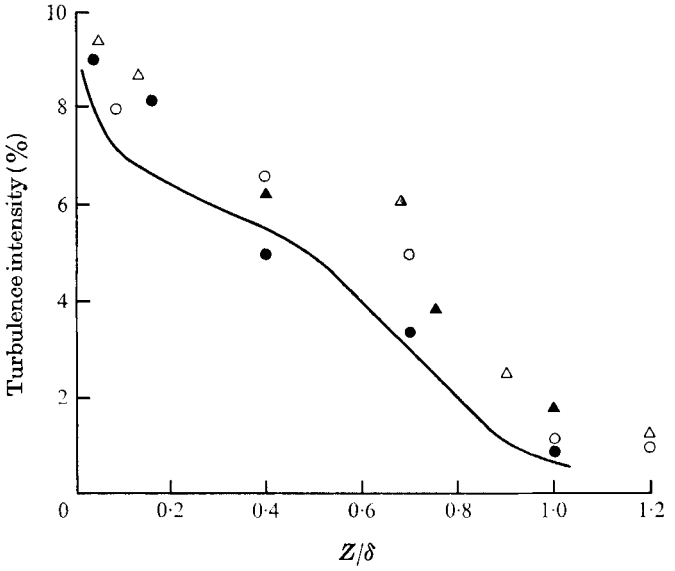

FIGURE 17. Variation of turbulence intensity (tangential component) across the boundary layer. ———, flat plate (Klebanoff 1955).

	○	△	●	▲
θ	170°	170°	300°	300°
R	0·92	0·82	0·82	0·92

5. New calculations

The radial velocity profile and wall shear-stress measurements, reported in §4, have revealed appreciable departure from the assumptions ((12)–(15)). In order to find the effect on the prediction of Θ_{11}, the following calculations were made.

The radial velocity profile (36), which is valid only in the outer region of the boundary layer, is not suitable for use in a momentum integral approach. The profile represented by

$$w = u\epsilon_m(1-z/\delta) \tag{50}$$

seems to fit the entire region (figure 9), where ϵ_m is the measured limiting streamline angle, which agrees with the values predicted using Mager's profile.

Here, the radial equilibrium equation (3) is redundant, since both the magnitude and the profile are assumed to be given by (50). If one incorporates these assumptions in (4)–(11), one obtains the following for Θ_{11} in the asymptotic region ($\partial/\partial\theta = 0$):

$$\frac{d\Theta_{11}}{dr} + 4\frac{\Theta_{11}}{r} = \frac{0{\cdot}0565}{\epsilon_m}\left(\frac{\Omega r^2}{\nu}\right)^{-\frac{1}{5}}, \tag{51}$$

whose solution is

$$\Theta_{11} = 0{\cdot}0122 \frac{r}{\epsilon_m} \left(\frac{\nu}{\Omega r^2}\right)^{\frac{1}{5}}; \tag{52}$$

in developing region ($\partial/\partial\theta \neq 0$), the equation corresponding to (24), with the new radial velocity (50) and wall shear stress (45), is

$$\frac{dF'}{d\theta} + 3{\cdot}22\epsilon_m F' - \frac{F'}{5\theta} = 0{\cdot}0296\,[1 + 0{\cdot}85\,(\epsilon\theta)^{\frac{1}{2}}], \tag{53}$$

where

$$F' = \frac{\Theta_{11}}{r} \left(\frac{\Omega r^2 \theta}{\nu}\right)^{\frac{1}{5}}. \tag{54}$$

Equation (53) is solved numerically, with the boundary condition $F' = 0$ at $\theta = 0$, and values of Θ_{11} are derived from (54). The results obtained are plotted in figures 3 (*a*), (*b*) for $R = 0{\cdot}55$ and $0{\cdot}72$. The trend is similar at other radii.

It is somewhat surprising that the values of Θ_{11} predicted by the previous calculation (§2, figures 3(*a*), (*b*)) show better agreement with the measured values than those predicted by this new calculation. The reason is that the assumed values for radial velocity (12)–(14) are lower than the measured values, and this has a tendency to over-predict Θ_{11}, where as the shear stress assumption based on stationary flat plate values, lower than the measured values in a rotating case, tends to predict lower values of Θ_{11}, so that, in combination, the two assumptions may cancel each other in this particular case, predicting results closer to the experimental values. But the new shear stress and radial velocity correlations should be used for meaningful prediction of the boundary-layer growth.

6. Concluding remarks

Thus, rotation-induced radial flow, however small it may be, substantially changes the characteristics of the boundary-layer growth along the blade, showing that two-dimensional calculations are inapplicable to cases of the sort under consideration.

The wall shear stress measurements indicate that the skin friction coefficients on a rotating blade are appreciably higher than those of a flat plate. The proposed skin friction correlations (45), (46), based on a larger number of measurements under a wide variety operating conditions, include not only the Reynolds number effect, but also the rotation effect R_0. Inclusion of the pressure gradient effects in these correlations would greatly enhance its practical value. If the effect of rotation is to increase the skin friction stress by 40–60 % at some blade locations, then its incorporation into the boundary-layer equations is obviously necessary. The turbulence intensities in the tangential direction are found to be generally higher than those of stationary flat plate. This is consistent with the shear stress measurements, at least qualitatively.

The applicability of the two-dimensional law of the wall to the tangential component of the three-dimensional boundary layer has been established; future efforts should be directed towards establishing a vectorial form of the law

of the wall and of the wake; they would necessarily include the gathering of much experimental data, in many different configurations. The cross-flow representation of Mager and Johnston may not yield an accurate account of radial flows on rotating blades: the three-layer model seems to provide a better insight into the phenomena. The outer layer profile can be represented by a relation such as (37), but the description of the collateral region and buffer layer needs further elaboration. The 'core' and 'interference' regions near the blade tip are strange new phenomena: complex interaction of radial flows with the annulus wall and its boundary layer has yet to be understood. Finally, the prediction of Θ_{11} and ϵ by the momentum integral method gives reasonably good results, but an improved radial velocity model would lead to even better predictions.

This work was supported by the National Aeronautics and Space Administration through the contracts NSG 537 and NGL 39-009-007, with technical management by W. R. Britsch of the NASA Lewis Research Center.

REFERENCES

BANKS, W. H. & GADD, G. E. 1962 *Nat. Phys. Lab. Rep.* SHR27/62.

BRADSHAW, P. 1971 *J. Fluid Mech.* **46**, 417.

BRADSHAW, P., FERRIS, D. J. & ATWELL, N. P. 1967 *J. Fluid Mech.* **28**, 593.

CHAM, T. S. & HEAD, M. R. 1969 *J. Fluid Mech.* **37**, 129.

FAGE, A. 1933 *Proc. Roy. Soc.* A **142**, 560.

FOGARTY, L. E. 1951 *J. Aero Sci.* **18**, 247.

HALLEEN, R. M. & JOHNSTON, J. P. 1967 *Rep.* MD18, Stanford University.

HORLOCK, J. H. & WORDSWORTH, J. 1965 *J. Fluid Mech.* **23**, 305.

JABBARI, A. 1969 M.S. Thesis, The Pennsylvania State University.

JOHNSTON, J. P. 1960 *Trans. A.S.M.E.*, D **82**, 233.

JOHNSTON, J. P. 1970 *Proc. Int. Symp. Fluid Mech. and Design Turbomachines*, The Pennsylvania State University. *N.A.S.A. S.P.* (To be published.)

KÁRMÁN, T. VON 1946 *N.A.C.A. Tech. Mem.* 1092.

KLEBANOFF, P. S. 1955 *N.A.C.A. Rep.* 1247.

LAKSHMINARAYANA, B. 1970 *Proc. Int. Symp. Fluid Mech. and Design Turbomachines*, The Pennsylvania State University *N.A.S.A. S.P.* (To be published).

MAGER, A. 1951 *N.A.C.A. Tech. Note*, 2310.

MCCAFFERTY, H. G. 1967 M.S. Thesis, The Pennsylvania State University.

MCCROSKEY, W. J. NASH, J. F. & HICKS, J. G. 1971 *A.I.A.A. J.*, **8**, 188.

MOORE, J. 1969 *Gas Turbine Lab. Rep.* 99, Massachusetts Institute of Technology.

NASH, J. F. 1969 *J. Fluid Mech.* **37**, 625.

PATEL, V. C. 1965 *J. Fluid Mech.* **23**, 185.

PIERCE, F. J. & KROMMENHOEK, 1968 *Interim Tech. Rep.* 2, Virginia Polytechnic Institute. (Also *DDC*, AD680973.)

PRAHLAD, T. 1968 *A.I.A.A. J.* **6**, 1772.

PRANDTL, L. 1946 *British M.A.P. R. & T.* 64.

PRESTON, J. H. 1954 *J. Roy. Aero. Soc.* **58**, 109.

RICHARD, E. J. & BURSTALL, F. H. 1945 *Aero. Res. Counc. R. & M.* 2126.

SCHLICHTING, H. 1960 *Boundary Layer Theory.* McGraw Hill.

WYNGAARD, J. C. & LUMLEY, J. L. 1967 *J. Sci. Instrum.* **44**, 363.